Direct Write Editing of Electronic Materials by Gas Assisted Focused Electron Beam Induced Etching for Device Prototyping

Technical Review and Proposal

Doctor of Philosophy in Material Science & Engineering

Branden Spencer Gellerup

September 2024

Committee Members:

Philip D. Rack (Chairperson)

Steven J. Randolph

Gong Gu

Dustin Gilbert

1. Background

1.1 Nanoscale Processing of Materials

Electronic devices typically necessitate silicon semiconductor chips, which are fabricated through wafer scale integrated circuit (IC) processing. The wafers are i) deposited with thin films of various types of materials, depending on the intended device, ii) coated with photo- or e-beam resist, iii) undergo lithography with deep ultraviolet light to develop the resist, iv) wet or dry etched, v) metallized with conductive electrical interconnects, and finally vi) cut into dies and packaged for device integration. IC fabrication is extremely time and cost intensive and is fine-tuned to produce billions of transistors, which makes IC processing incompatible with rapid materials prototyping for finding and assessing the next generation of materials and devices.

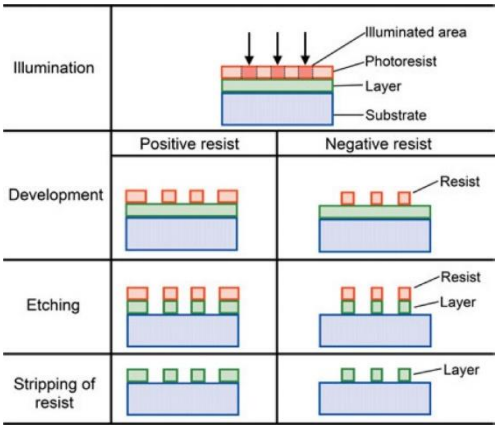


Figure 1. Illustration of lithographic patterning of positive and negative resist.[1]

To assist in the rapid prototyping and small scale manufacturing, direct-write processes have been developed. Recently meso to macro scale 3D printing of materials has burgeoned, micro to nanoscale direct write patterning is more challenging. Focused and scanned lasers can be utilized for both direct-write and ultrafast processing of materials for developing thin film

materials. Lasers can be i) additive through laser induced depositions, ii) subtractive through ablation, and/or iii) transformative through thermal annealing or crystallization.

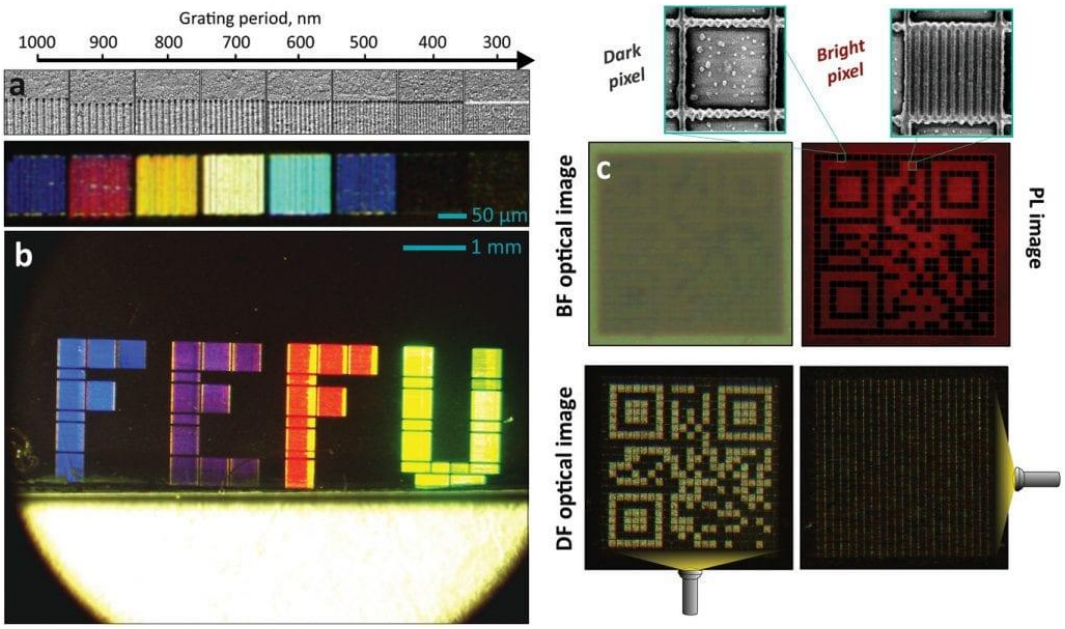


Figure 2. Example of nanoscale laser processing of perovskites.[2]

Laser processing offers high throughputs and can offer wide area mask-free patterning but are limited in focal spot diameters on the scale of ~1 µm and are limited in materials that can be coupled thermally/optically to the laser wavelength or are not physically degraded from laser exposure.

Ions can likewise be used for rapid prototyping, and can be applied for i) material deposition, ii) material removal whether through sputtering or chemical reactions such as in reactive ion etching (RIE), and iii) implantation for modifying material properties.

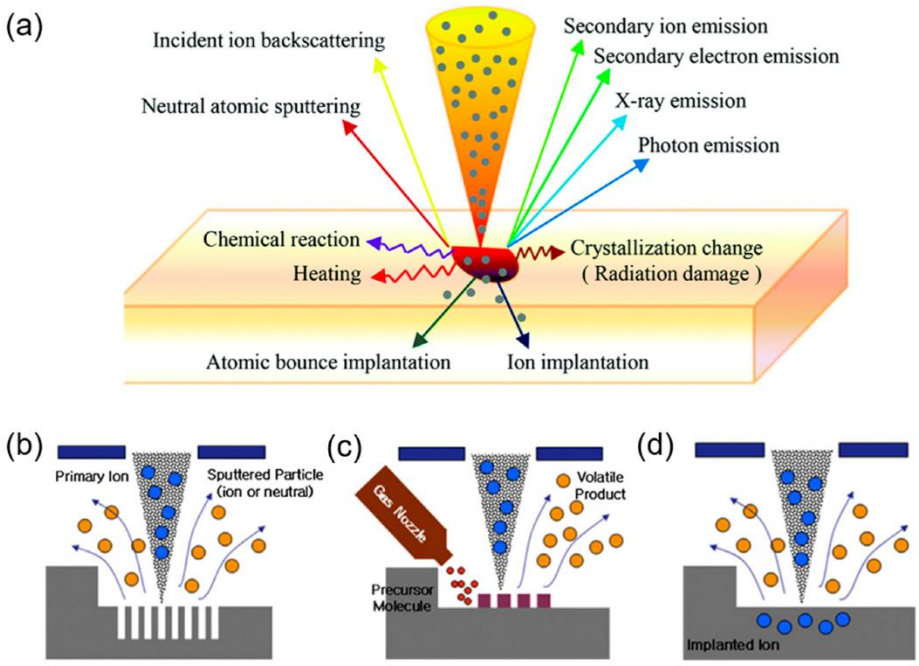


Figure 3. Nanoscale ion beam interactions and processing.[3]

However, ion beams can lead to sub-surface damage such as amorphization or defect formation and have a larger spot size than electrons.

1.2 FEBIE

Focused electron beam induced etching (FEBIE) is a nanoscale direct-write technique which involves an electron beam stimulating the dissociation of surface-adsorbed precursor gases into byproducts, which react with the surface of the film/substrate. Special precursors are designed such that the byproducts/film reaction product is volatile and thus desorbs (sometimes upon further electron stimulation) and are pumped out of the chamber, leading to removal of the film/substrate. This is akin to the more studied focus electron beam induced deposition (FEBID), or if also using a pulsed laser for thermal assist, laser-assisted electron beam induced deposition (LAEBID), where the gas assist produces a byproduct which condenses to the film/substrate such as for depositing platinum,[4-7] gold,[8] tungsten,[9-11] and chromium.[11]

Low-energy electron beams (<30 keV) generally are insufficient for inducing knock-on events due to the relatively small mass of electrons. Judicious control of both electron beam parameters and gaseous precursor can lead to highly selective editing whereas electrons requiring a gas-assist from a chemical precursor for FEBIE, and at gas precursor pressures below the threshold of spontaneous etching an electron is required to selectively stimulate reactions. The chemical nature of this process renders it comparatively "soft" compared to the collateral damage of ion implantation, defect generation, and lattice disruption/amorphization induced from focused ion beam (FIB) knock-on sputter removal or chemically enhanced sputtering processes of FIB milling.

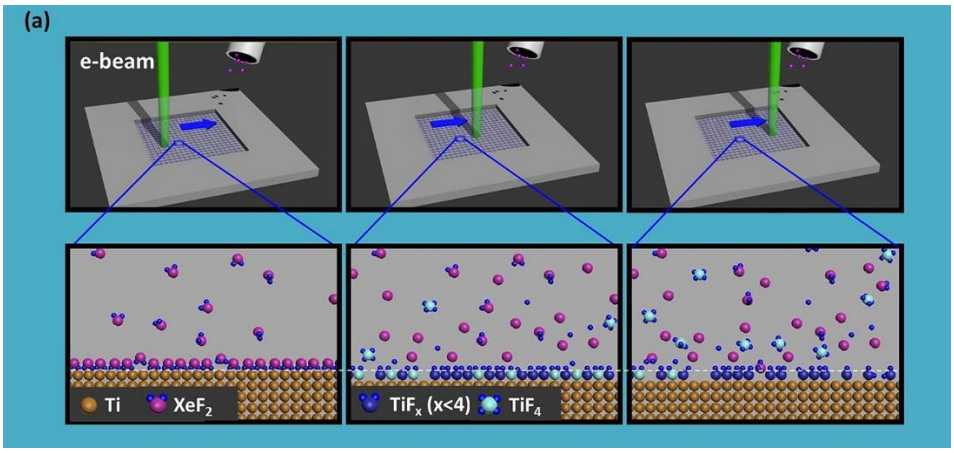


Figure 4. FEBIE of titanium with XeF_2 precursor.[12]

Examples of gaseous precursors used as gas-assists in FEBIE are H_2O,[13] O_2,[14] Cl_2,[10, 15-16] F_2,[10] ClF_3,[10] and nitrosyl chloride.[17] Another common vapor phase precursor is XeF_2, which has been used for the FEBIE of silicon and silicon dioxide,[10, 15-16, 18] silicon nitrides,[16, 19-20] tantalum nitride,[21] PMMA,[10] gallium arsenide,[10, 22] titanium,[23] chrome,[24] and recently molybdenum disulfide.[25] Upon electron stimulation, adsorbed XeF_2 undergoes dissociation via homolytic cleavage that forms fluorine radicals which can be represented by Eq. (1):

$$XeF_2 + e^- \rightarrow Xe + 2F + e^- \quad (1)$$

XeF_2 can also etch some materials spontaneously without electron exposure, such as in the case of silicon,[26] and measures must be taken to prevent this, such as finding a working pressure below the spontaneous etching threshold, passivating the surface of your film,[21] or limiting overall XeF_2 exposure outside of the intended etching region of interest.

1.3 Superconductivity

Dr. Heike Onnes discovered a phenomenon in mercury in 1911 known as superconductivity, where certain materials resistivity effectively decreases to zero below a critical temperature T_C. Using quantum mechanical framework, a mathematical model of superconductivity called the Ginzburg-Landau theory was developed in 1950, which matched macroscopic measurements, but did not function at the microscopic level or explain the phenomenological behavior of superconductors. A theory which could both accurately predict and justify superconductors behavior at both the micro- and macroscopic levels was not formulated until 1957 by Barden, Cooper, and Schrieffer, known as BCS theory. They hypothesized the existence of pairs of electrons with opposite spin and motions, which bond at temperatures low enough where Coulombic force is negligible, leading to quantum mechanical quasi-particles called Cooper pairs which have strong electron–phonon interactions. However, over time materials with higher T_C have been sought after and discovered, which BCS theory fails to explain as electron–phonon interactions are quenched at higher temperatures. Cooper pairs are hypothesized to form at higher temperatures through electron-atom interactions

called “spin waves” where Cooper pairs are formed by the spins of electrons coupling with the spins of atoms.

Superconductors additionally repel all magnetic field lines below the surface when cooled below their T_C, which is referred to as the Meissner effect and leads to the behavior of magnetic levitation of superconductors. The London penetration depth is the length a magnetic field line enters a sample before being repulsed and is characteristic to each superconductor. The London penetration depth is a function of temperature, and above T_c the magnetic field fully penetrates the sample and disrupts superconductivity. The applied magnetic field can also kill superconductivity at a critical field strength, H_C, and superconductors are classified into two types based on their behavior past this H_C. Type I superconductors lose their superconductivity abruptly above their H_C, whereas Type II superconductors have two transitions, H_{C1} and H_{C2}, with an intermediate state between where a gradual transition from superconductivity to non-superconducting due to localized superconducting regions called vortices. Similarly, there is a critical electric current density, J_C, where at sufficient currents the magnetic field induced by the current is greater than H_C, killing superconductivity.

1.4 Superconducting Devices

1.4.1 Josephson Junctions

Josephson junctions are channels of superconducting materials with a barrier in between known as the weak link. The types of junctions are defined by the barrier material. The barrier can be a non-superconducting metal (denoted by ‘N’) for a S-N-S junction, an insulator (denoted by ‘I’) for a S-I-S junction, or by reducing the superconducting channel geometry through

constriction (denoted by 'C') for a S-C-S junction where Dayem bridges are a type of S-C-S where the channel is a wire. Weak links can also be created by damaging a region of the superconductor to the point of quenching superconductivity, such as through ion implantation and defect generation. Cooper pairs have a coherence length (ξ), or a distance they remain bonded, which is the wavefunction width of the Cooper pair, and if this coherence length is larger than the barrier width then there is a probability of the Cooper pair tunneling across the weak link, similar to standard electron tunneling.

The weak link barriers are typically a few nanometers thick in tri-layer Josephson junctions or less than one micron wide for S-N-S barriers. *De Leo et. al* reports forming nanoconstrictions through Ga+ ion beam milling to thin niobium films and create 200 nm wide trenches.[27] Sub-100 nm junction widths have been reported using EBL within the last decade.[27-28] The smallest Nb junction width reported has a minimum bridge area of 65 nm in width and 60 nm in length.[27] *Bouchiet et. al* reports fabricating Dayem bridges by locally anodizing 50 nm wide strips between 3 nm thick niobium to thicken the oxide with an AFM voltage-biased tip.[29] However, using this AFM tip anodizing method your film thickness must be less than the typical depth of oxidized metal (~10 nm) in order to fabricate the structure in a single step, where the T_C of niobium decreases with decreasing thickness below 200 nm and approaching 6 K for few nanometer thick films. A desired Josephson junction barrier width for a full barrier cavity is less than the coherence length, which is 38 nm for niobium.

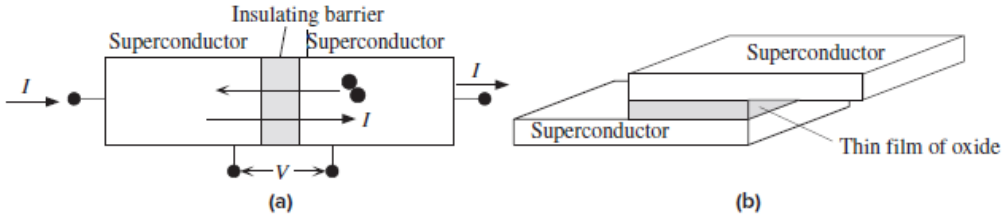


Figure 5. Illustrations of a) lateral and b) stacked S-I-S Josephson junctions.[30]

The Josephson effect is the direct current (DC) or supercurrent, *I*, produced from the spontaneous tunneling of Cooper pairs across the weak link, where the supercurrent depends on the degree that the phase angle (θ) of the wavefunction changes across the barrier described by Eq. (2):

$$I = I_C \sin(\theta) \tag{2}$$

where I_C is the critical current, and for currents $>I_C$, I/I_C is greater than one, and thus the phase angle of the wavefunction for the tunnelling Cooper pair is not possible. For currents $>I_C$ a current still passes through the Josephson junction but instead of tunneling Cooper pairs, it occurs by standard electron tunnelling. These function as “on” and “off” states that exhibits hysteresis and has switching times of ~10 ps. The Josephson effect applies when an alternating current (AC) is produced from applying a voltage across the junction, but the current is affected by a new phase angle changed by the applied voltage which changes the AC frequency, *f*, based on Eq. (3):

$$f = \frac{2eV}{h} \tag{3}$$

where *e* is the elementary charge of an electron, and h Is Planck's constant. Notice the lack of any material properties in Eq. (3), meaning Josephson junctions producing an alternative current acts as a voltage-to-frequency converter (VFC).

1.4.2 SQUID

Superconducting quantum interference devices (SQUID) are devices made of coils or loops of superconducting material with Josephson junctions. There are two types of SQUID devices, i) DC SQUIDs which are made of a loop with two Josephson junctions each and utilize the DC Josephson effect, and ii) RF SQUIDs which use only one Josephson junction and utilize the AC Josephson effect. SQUIDs have applications in magnetometry for measuring incredibly low magnetic fields and can be added onto AFM cantilever probe tips and are also being evaluated for logic circuits to make quantum bits (qubits) in quantum computing.

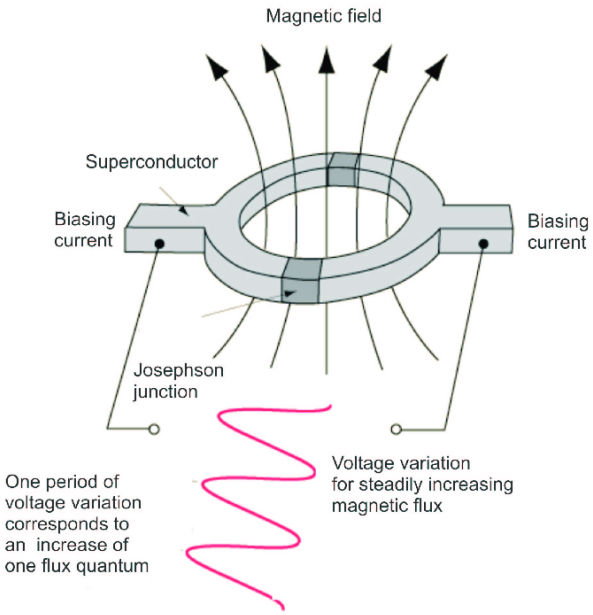


Figure 6. Depiction of DC SQUID device and operation.[31]

SQUIDS are typically made of pure niobium for low T_C applications and can also be made of Nb thin films. The thin films are typically deposited via sputtering or e-beam evaporation, and

then the Josephson junctions are formed by standard lithographic patterning, followed by reactive ion etching (RIE) in fluorine chemistries such as SF_6 or CF_4, and then finally making the weak link barrier by depositing an insulator such as AlO_x[32] for making a S-I-S, depositing metal such as Al[33] or Au[34] for a S-N-S, or cutting constrictions into niobium. Niobium Dayem bridge based SQUIDs have been reported with a spin sensitivity of 60 spin/$Hz^{1/2}$ and a magnetic flux noise spectral density of 1.5 $\mu\Phi_0/Hz^{1/2}$.[35]

1.5 2D Materials

1.5.1 Transition Metal Dichalcogenides

Transition metal dichalcogenides (TMDs) are semiconducting materials with the chemical stoichiometry of MX_2, where M is a transition metal and X is a chalcogenide. They have drawn considerable interest based on their 2D forms and are a type of Van der Waals materials, which is a class of 2D materials where in-plane atoms have covalent bonding and out-of-plane atoms are held in place by weak Van deer Waals forces. The most popular TMDs are molybdenum and tungsten sulfides MoS_2 and WS_2, and selenides $MoSe_2$ and WSe_2, where thin films are grown via PVD methods such as sputtering and pulse laser depositions (PLD), or chemical vapor deposition (CVD) and atomic layer deposition (ALD). TMDs can be used in their amorphous forms but are commonly used in their 2H (hexagonal) or 1T crystalline phases, which are semiconducting and metallic, respectively. Phase transitions of TMDs are a substantial reason for their intrigue, as their properties can be changed based on thermal inputs, such as a transition from insulating amorphous phase to semiconducting 2H phase through thermal annealing.[36-37]

TMD monolayers offer a tantalizing combination of electronic, optical, and mechanical properties. Electronically they possess a high charge carrier mobility with efficient charge transfer,[38] 2-3 times faster radiative recombination than their bulk counterparts,[39] and have low power requirements with high on/off ratios for circuits and FETs.[40-41] TMDs can display both n- or p-type behavior,[42] be substitutionally doped,[43] and be manipulated via defect engineering[44-45] Optically several TMDs shift from an indirect to direct band gap based on thickness with band gaps typically ranging from 1.7-2 eV which sits within the visible spectrum.[46-47] Mechanically they are highly stretchable and bendable and strain tunable.[48] TMDs have a wide array of applications, such as transistors,[49-50] photodetectors,[51-52] chemical sensors,[53-55] and chemical catalysts.[56-58]

1.5.2 Heterostructures

Heterojunctions are when dissimilar semiconducting materials are joined together either where atomically thin layers can be stacked vertically or placed in-plane horizontally.

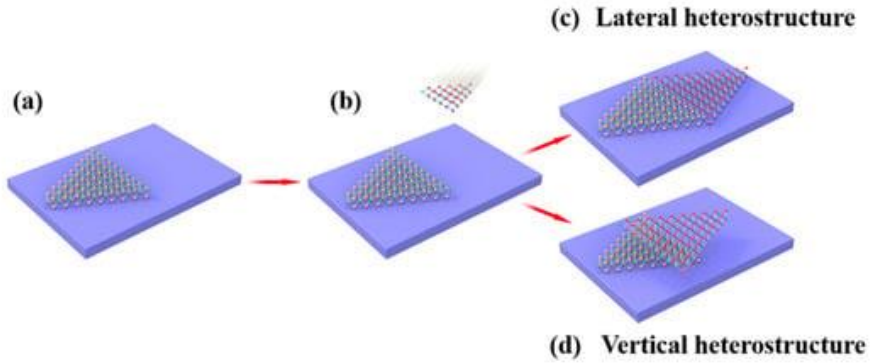


Figure 7. Illustration of lateral and vertical heterostructures.[59]

Combinations of different materials can be used to tune properties and performance, and disparate classes of materials such as semiconductors and insulators can be integrated into quantum well structures with enhanced electrical and optical properties. These combined 2D

materials can produce distinct phenomena which cannot be replicated from just one of the constituent materials. Heterostructure devices are crucial for developing the next-generation of energy efficient electronics.

1.6 Characterization Methods

1.6.1 Scanning Electron Microscopy

The scanning electron microscope (SEM) source, or electron gun, is a filament with a microscopic tip that is typically made of tungsten that acts as a Schottky emitter when sufficiently biasing the tip with a high voltage and emission current in a high vacuum. The emitted electrons travel through the electron column where they are collimated into a beam by condenser lenses, restricted to a certain diameter through an objective aperture, and aligned by deflection coils. The electron beam enters the sample chamber and interacts with the sample, where an SEM image is collected where the rastered beam is correlated to electrons that are either backscattered or induced by secondary electron generation in the material.

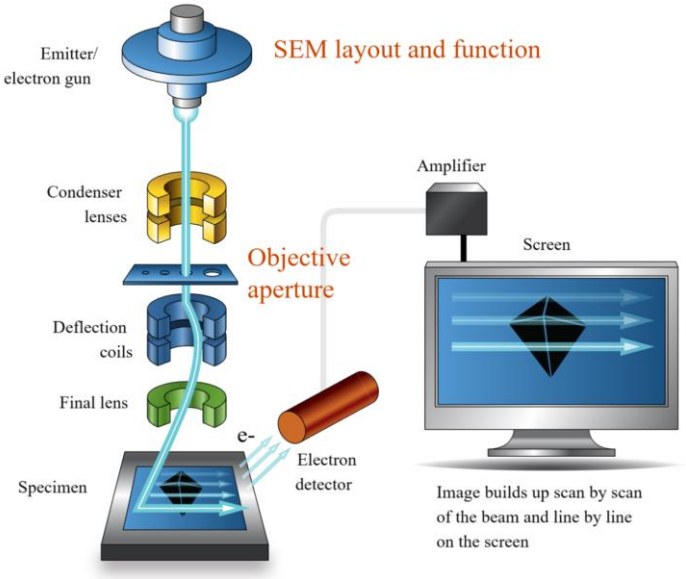


Figure 8. Diagram of SEM microscope.[60]

Electron microscopes can be coupled with energy dispersive spectroscopy (EDS), where the electron beam from the SEM excites the sample to emit x-rays, which are characteristic to chemical elements and are used to identify the chemical composition of the sample when collected by an x-ray detector.

1.6.2 Atomic Force Microscopy

An atomic force microscope (AFM) is an instrument that can image specimens through the use of an AFM probe, which is comprised of a cantilever with a tip protruding down on one end. A laser is focused near the tip-end of the cantilever, and is reflected into a photodetector. An AFM image is produced when the tip is either tapped or dragged in-contact along the samples surface below it. As the tip is attracted or deflected by the sample's surface, the laser position on the cantilever changes, and thus the vertical position of the sample height is correlated to the is reflected laser spot on the photodetector. Thus, height maps with sub-nm resolution can be generated via a 2D scan and correlation of the laser's reflected position on the photodetector.

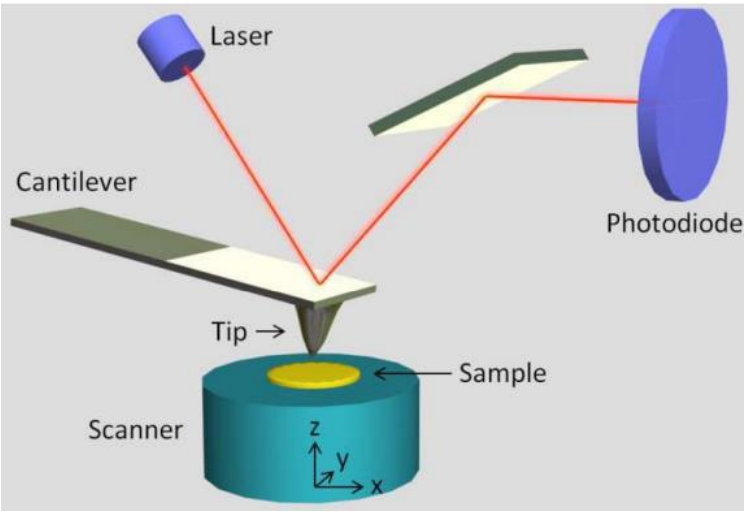


Figure 9. Diagram of AFM system.[61]

1.6.3 Raman/Photoluminescence Spectroscopy

When light impinges upon a molecule, the photons can interact with the molecule in two ways, i) be elastically scattered, known as Rayleigh scattering, or ii) be inelastically scattered, known as Raman scattering, where the energy of the photon changes. The photon is absorbed by the molecule, exciting the molecule into a new vibrational phonon mode, and then is instantaneously re-emitted with a different energy value. When the Raman scattered photon has less energy than that of the impinging light it is known as a Stokes shift, and when it gains energy, it is known as an Anti-Stokes shift. The Raman shift is the difference in wavenumber between the Raman scattered photons and the Rayleigh scattered photons and is equal to the vibrational transition energy used by the molecule. This definition is used such that all wavelengths of impinging light can be used to produce the same Raman shift. Raman spectra are acquired by placing a sample under a laser beam and directing the scattered laser light upon a grating which acts as a prism to disperse the light and increases the resolution for a given wavelength range, where the dispersed light is collected via a CCD detector. Raman scattering is the basis of Raman spectroscopy, where the Raman scattering event is used as a “fingerprint” for the material that caused the scattering event based on the vibrational phonon modes of the material itself. The Raman spectra is used to identify types of materials, phases, and defects as well as measuring sample crystallinity and strain.

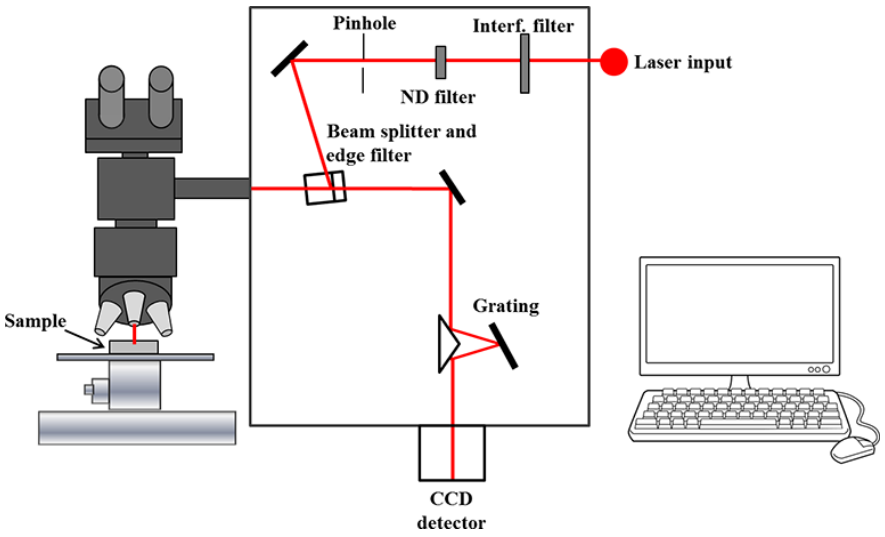


Figure 10. Diagram of Raman spectrometer.[62]

Photoluminescence (PL) spectroscopy is similar to Raman spectroscopy where light is irradiated on material which leads to the emission of photon with a shift in wavelength. However, during PL the photon is absorbed and thus is wavelength dependent and involves an electronic transition rather than vibrational. The original light excites an electron in the irradiated material to the conduction band, leaving an electron hole in the valence band. This electron-hole pair can be bound by coulombic attraction and are defined as a quasiparticle known as an exciton. When the electron relaxes back to its valence band (ground state) it can emit a photon equal to the energy between those states through the radiative recombination of the exciton. Bright excitons with opposite spin in the electron-hole pair can easily radiatively recombine and contribute to PL, where dark excitons have the same spin in the electron-hole pair and do not conserve spin momentum for recombination. PL occurs only in direct band gap semiconductors or other materials with impurity states that are optically active. 2D material's additional spatial confinement enhances exciton motion and attraction, allowing for optical exciton peaks with long lifetimes at room temperature and introduces new exciton interactions.

Excitons sit within valleys of the electronic band structure, or the local extremum of the valence and conduction bands. Transitions can occur for multiple different valleys, leading to different exciton peaks in the PL spectra.

2. Proposal

Chapter 1. Niobium FEBIE

Introduction:

Pure elemental niobium is a type-I superconductor with the highest superconducting transition temp (T_C) for all pure metals, of 9.33 K and upper critical magnetic field (H_{C2}) of 4020 Oe.[63], where impurities are known to shift the material to a type-II semiconductor.[64] Niobium can be etched in fluorine chemistries, such as with $CBrF_3$, CF_4, and SF_6 precursors with reactive ion etching (RIE).[65] Given this, it is hypothesized that niobium could be etched by a XeF_2 precursor via an electron stimulated process. A possible XeF_2 reaction pathway involving Nb is the generation of volatile niobium pentafluoride as in Eq. (1).[12, 19, 21-22, 66]

$$5XeF_2 + e^- + 2Nb \rightarrow 5Xe + 2NbF_5 \quad (1)$$

Utilizing XeF_2 as a gas-assist with FEBIE to etch niobium films is an attractive alternative nanoscale direct write method to standard focused ion beam sputtering. Superconducting devices could be fabricated by etching gaps to form Josephson junctions. The gap in superconductor channels are in sub-micron size, where sub-100 nm junction widths have been reported using EBL within the last decade,[27-28] where the smallest niobium junction width

reported has a minimum bridge area of 65 nm in width and 60 nm in length.[27] A desired Josephson junction barrier width is less than the coherence length, ξ of 38 nm for niobium.

Proposed work:

We propose investigating if niobium thin films can be etched via FEBIE using gaseous XeF_2 precursor in an SEM equipped with a GIS needle, and whether line etches can etch features with widths narrower than the 38 nm coherence length of niobium. Niobium films will be magnetron sputtered onto silicon oxide coated silicon wafers, where the oxide film conveniently acts as a barrier to spontaneous Si etching once FEBIE of niobium is complete. The electron beam current, beam energy, and dwell time will be varied to determine their effect on the FEBIE of niobium and the resolution of line etches. AFM and SEM measurements will be taken post etching to determine etch depths, which will be correlated with end-point monitor graphs (EPM) to determine the dose-to-clear (all niobium removed down to SiO_2 layer) for various conditions. Etch rates and efficiencies will be calculated from the etch depths or dose-to-clear to find the optimal FEBIE parameters. The presence of niobium spontaneous etching by XeF_2 will be identified, and if present the dependency of XeF_2 chamber working pressure and total etch area on the spontaneous etch rate will be established. Additionally, we will determine the etch rate efficiencies as a function of all of the parameters to elucidate and model the Nb + XeF_2 + e- FEBIE process.

Finally, we will fabricate Nb 4-point probe devices via patterning the Nb magnetron sputtered film with an SF_6-O_2 plasma. FEBIE channels of various widths and lengths will be

etched into the devices to make Josephson junctions and their properties measured via a Physical Properties Measurement System (PPMS) system.

Preliminary results have confirmed that niobium can be etched by XeF_2 assisted FEBIE. AFM results in **Fig. 1 a-b)** demonstrate the etch depth as a function of time (dose) at two currents (0.025 and 0.1 nA) are correlated to the progressions of the topography and EPM graphs shown in **Fig. 2 a-b)**.

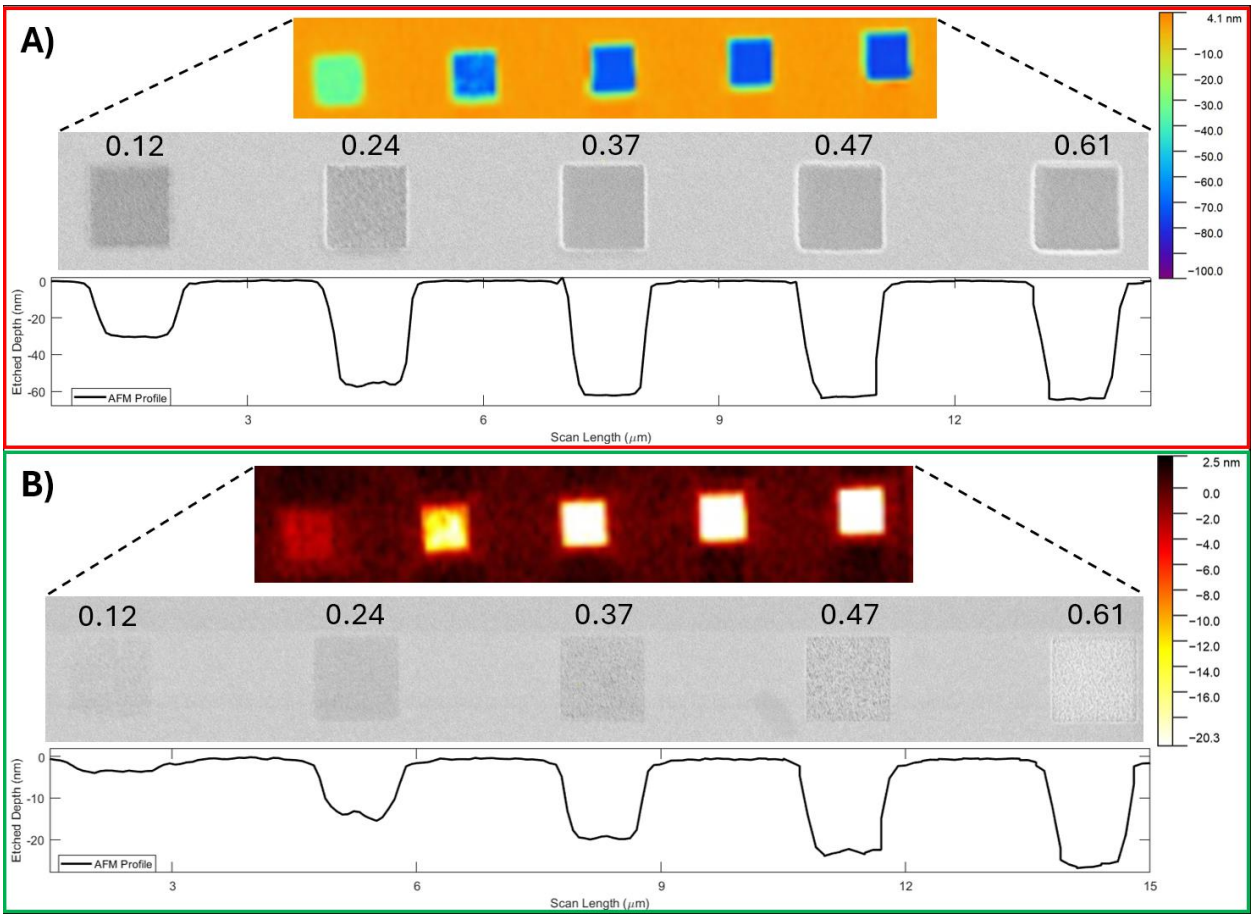


Figure 1. Gas-assisted FEBIE of 1 μm^2 box etches were conducted at a beam energy of 1 keV, dwell time of 1 µs, pixel pitch of 10 nm, XeF_2 working pressure of $1x10^{-5}$ Torr, varying beam currents from 0.025 – 0.8 nA where A) SEM images are correlated with AFM images and line profiles for beam current of 0.025 nA, and B) 0.1 nA box series.

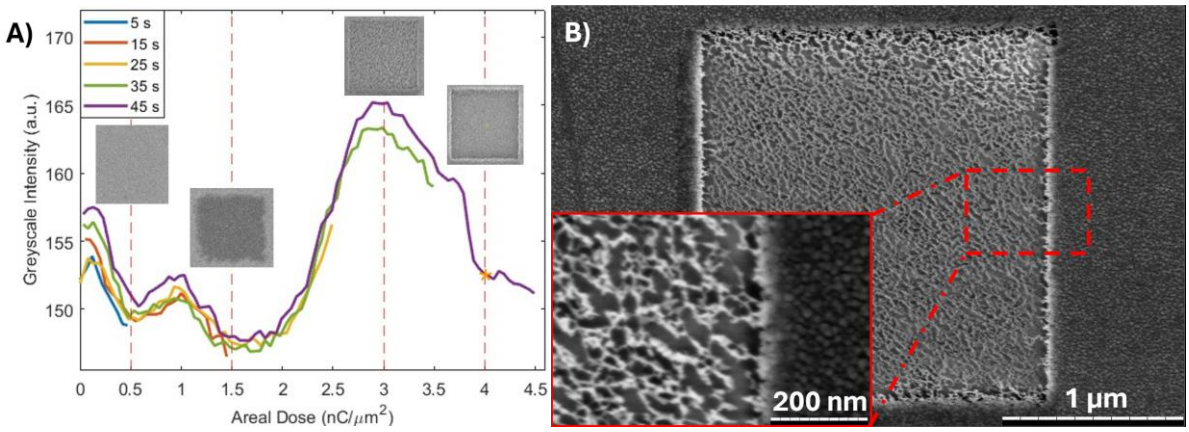


Figure 2. Gas-assisted FEBIE of 1 μm^2 box etches were conducted at a beam energy of 20 keV, 0.025 µs dwell time, pixel pitch of 10 nm, and XeF_2 working pressure of $4.7x10^{-6}$ Torr. A) illustrates a series of EPM graphs for FEBIE experiments run at 0.1 nA to various times (insets are SEM images taken at those dose/times which correlates the etch progression to the EPM signatures, where 4 nC/μm^2 is the dose-to-clear. B) SEM images of roughness induced from non-cleared 5 second etch.

Chapter 2. WS_2 FEBIE

Introduction:

Advanced nanoscale processing of TMD materials and devices is necessary for wide-spread implementation. In particular, direct-write selected area techniques such as FEBIE can enable fast device prototyping capabilities that accelerate discovery. WS_2 can be etched by XeF_2 precursor gas, and at localized pressures much higher than experienced during FEBIE, spontaneous XeF_2 layer thinning and doping has been demonstrated for WS_2[67] and WSe_2.[68]

Recently, *Lasseter et. al* conducted XeF_2 gas-assisted FEBIE on both MoS_2 exfoliated flakes and CVD grown monolayer films.[25] Likewise, Raman and Photoluminescence spectroscopy was used in tandem with STEM analysis where the findings established this gas-assisted process is relatively “delicate” and higher resolution compared to ion-based milling. Raman spectroscopy indicated that the surrounding and sub-surface unetched material

experienced little peripheral damage based on a no associated change in the LA(M) disorder mode, and STEM revealed that the etched feature was <40 nm wide. Raman spectroscopy and STEM revealed the formation of point defects such as sulfur vacancies during etching, which extend to form nanopores, which agglomerate laterally across the surface as etching progresses. FET devices with MoS_2 monolayer channels were created and edited using FEBIE, where the channel width was narrowed post-device synthesis. Furthermore, sub-etching exposures were performed and enhanced n-type conduction was revealed, presumably due to the generation of sulfur vacancies.

Proposed work:

We propose to investigate the XeF_2 assisted FEBIE of WS_2, similar to what *Lasseter et. al* did with MoS_2. Multilayer WS_2 will be created by mechanical exfoliation of bulk crystals using tape transfer onto gold coated substrates, which conveniently do not etch by XeF_2 FEBIE so is a robust etch stop layer. Furthermore, monolayer WS_2 flakes will be grown by CVD and wet transferred onto gold-coated substrates. The WS_2 samples will be etched under varying electron beam current, beam energy, and dwell time. Raman spectroscopy will be used to correlate any sub-surface damage generated via the FEBIE process. The sample thickness and FEBIE etch depths will be measured AFM to calculate etch rates and efficiencies. Line etching parameters will be optimized to realize the highest etching resolution. Back-gated (SiO_2) WS_2 thin film FETs will be fabricated and the channels narrowed via the optimized FEBIE etching process into channels with various channel widths. FET device electronic measurements will be collected to compare electronic properties to FET devices fabricated via the FEBIE method. Photoluminescence and Raman spectroscopy will be measured on the monolayer films to

determine the dose-to-clear and elucidate information on the evolving monolayer during etching. Monolayer WS_2 will additionally be transferred onto quantifoil TEM grids and undergo XeF_2 FEBIE, then imaged by STEM to identify the etch evolution and peripheral damage induced in the near etch region.

Preliminary results of XeF_2 gas-assisted FEBIE of WS_2, WSe_2 and MoS_2 exfoliated flakes were initially performed with areal doses ranging from 2-40 nC/µm^2 where SEM images of each flake are pictured in **Fig. 1a-c)** and etch depths were measured via AFM to establish generalized etch rates for each TMD in **Figure 1d)**. Volumetric etch rates and efficiencies were extrapolated from the slope of these depth vs dose plots and tabulated in **Table I**.

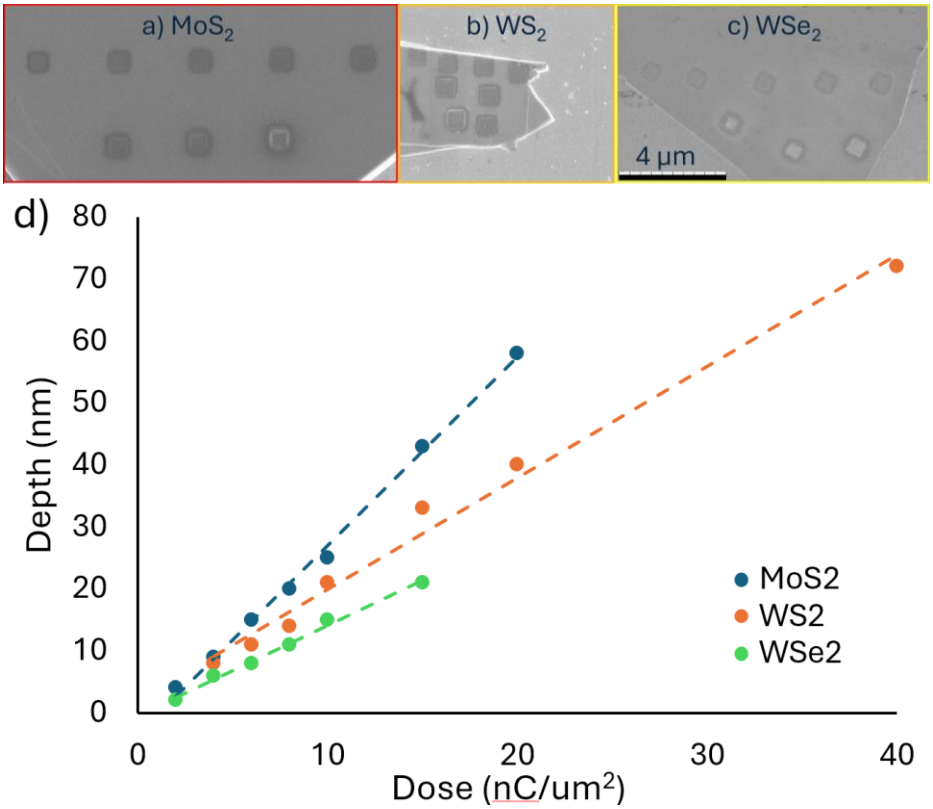


Figure 1. Gas-assisted FEBIE of 0.25 µm^2 box etches were conducted on a) MoS_2 and b) WS_2 for doses between 2-40 nC/µm^2, and c) WSe_2 for doses of 2-15 nC/µm^2 using a beam energy of 5 keV, beam current of 0.4 nA, single pixel dwell time of 0.1 µs, pixel pitch of 1 nm, and

XeF_2 working pressure of $2x10^{-6}$ Torr. d) Illustrates volume of TMD material etched via FEBIE vs total areal dose

Table I. Average FEBIE etch rate and etch efficiency for each TMD type

Material	Rate ($\mu m^3/s$)	Efficiency ($\mu m^3/nC$)
MoS_2	$1.21x10^{-3}$	$4.86x10^{-4}$
WS_2	$7.20x10^{-4}$	$1.80x10^{-3}$
WSe_2	$1.46x10^{-3}$	$5.82x10^{-4}$

Chapter 3. TMD Heterostructure

Introduction:

TMD heterostructures, most commonly MoS_2-WS_2, can be fabricated into devices such as top-gated field effect transistors[69] and photodetectors.[70] MoS_2-WS_2 exhibits strong interlayer coupling and efficient interlayer charge transfer,[71-72] and shows better electrical and optoelectronic properties than either of the constituent materials.[73] These heterostructures are typically grown via CVD, either by growing each constituent material then using wet/dry transfer to assemble, or by using a one-[74-75] or two-step[76] growth process. Without the use of lithographic patterning before growth, the CVD grown flakes self-assemble into dodecahedron, hexagonal, or triangular shapes[77] and the assembled heterostructures will likewise remain in the same shape.

Through the use of gas-assisted FEBIE, the heterostructures can be edited into novel on-the-fly shapes and structures, such as in the case of creating a FET device where the conductive channel length and width can be defined by etching away the surrounding material. Manipulating morphology and anisotropy can be used to tune the devices electronic and optoelectronic properties.[78] Etching features such as lines, holes, or trenches could be used to

strain the device or for defect engineering such as forming edge sites which affect the electronic properties of the device.[77]

Proposed work:

Single-layer MoS_2 and WS_2 will be grown via CVD, and wet-transferred via a PDMS support, then viscoelastically stamped to form the vertical heterostructures. FEBIE using XeF_2 gas-assist will be utilized to edit the geometry of the heterostructures by selectively etching away the surrounding material. Raman and photoluminescence spectroscopy and AFM imaging will be used to determine the dose-to-clear. Contacts will be deposited through standard photolithography processes to fabricate a back-gated FET device or photodetector. Electrical/optoelectronic measurements will be collected, and the performance of the edited devices will be analyzed.

References

[1] A. Ostendorf, and K. König, in *Tutorial: Laser in material nanoprocessing*, De Gruyter, Berlin 2015, Optically Induced Nanostructures: Biomedical and Technical Applications. https://www.ncbi.nlm.nih.gov/books/NBK321721/figure/oin_tutorial.F5/

[2] A.Y. Zhizhchenko, P. Tonkaev, D. Gets, A. Larin, D. Zuev, S. Starikov, E.V. Pustovalov, A.M. Zakharenko, S.A. Kulinich, and S. Juodkazis, *Small*, 2020, **16**, 2000410. **https://doi.org/10.1002/smll.202000410**

[3] L. Zhao, Y. Cui, J. Li, Y. Xie, W. Li, and J. Zhang, *Nanomaterials*, 2023, **13**, 1839. https://doi.org/10.3390/nano13121839

[4] M.G. Stanford, B.B. Lewis, J.H. Noh, J.D. Fowlkes, N.A. Roberts, H. Plank, and P.D. Rack, *ACS Appl. Mater. Interfaces*, 2014, **6**, 21256–21263. https://doi.org/10.1021/am506246z

[5] M.G. Stanford, B.B. Lewis, J.H. Noh, J.D. Fowlkes, and P.D. Rack, *ACS Appl. Mater. Interfaces,* 2015, **7**, 19579–19588. https://doi.org/10.1021/acsami.5b02488

[6] N.A. Roberts, J.D. Fowlkes, G.A. Magela, and P.D. Rack, Nanoscale, 2013, **5**, 408. **https://doi.org/10.1039/C2NR33014H**

[7] J. Lasseter, P.D. Rack, and S.J. Randolph, *ACS Appl. Nano Mater.* 2022, **5**, 10890-10899. https://doi.org/10.1021/acsanm.2c02182

[8] J. Lasseter, P.D. Rack, and S.J. Randolph, *Nanomaterials,* 2023, **13**, 757. **https://doi.org/10.3390/nano13040757**

[9] N.A. Roberts, C.M. Gonzalez, J.D. Fowlkes, and P.D. Rack, *Nanotechnology*, 2013, **24**, 415301. **DOI** 10.1088/0957-4484/24/41/415301

[10] S. Matsui, T. Ichihashi, and M. Mito, *J. Vac. Sci. Technol. B*, 1989, **7** 1182–90.

[11] S. Matsui, and K. Mori, *J. Vac. Sci. Technol. B*, 1986, **4**, 299–304.

[12] J.H. Noh, J.D. Fowlkes, R. Timilsina, M.G. Stanford, B.B. Lewis, and P.D. Rack, *ACS Appl. Mater. Interfaces*, 2015, **7**, 4179–4184. https://doi.org/10.1021/am508443s

[13] K.T. Kohlmann-von Platen, and W.H. Brunger, *J. Vac. Sci. Technol. B,* 1996, **14**, 4262.

[14] D. Wang, P.C. Hoyle, J.R.A. Cleaver, G.A. Porkolab, and N.C. MacDonald, *J. Vac. Sci. Technol. B*, 1995, **13**, 1984–1987. https://doi.org/10.1116/1.588119

[15] S. Wang, Y.-M. Sun, J. M. White, A. Stivers, and T. Liang, *J. Vac. Sci. Technol. B, 2005,* **23**, 206. doi: 10.1116/1.1848107

[16] J.W. Coburn and H.F. Winters, *J. Appl. Phys.,* 1979, **50**, 3189.

[17] T. Bret, B. Afra, R. Becker, Th. Hofmann, K. Edinger, T. Liang, and P. Hoffmann, *J. Vac. Sci. Technol. B,* 2009, **27**, 2727. doi: 10.1116/1.3243208

[18] R.R. Kunz and T.M. Mayer, *J. Vac. Sci. Technol. B,* 1987, **5**, 427.

[19] M. Yemini, B. Hadad, Y. Liebes, A. Goldner, and N. Ashkenasy, *Nanotechnology*, 2009, **20**, 245302. DOI 10.1088/0957-4484/20/24/245302

[20] Y. Liebes, B. Hadad, and N. Ashkenasy, *Nanotechnology,* 2011, **22,** 285303. **DOI** 10.1088/0957-4484/22/28/285303

[21] M.G. Lassiter, T. Liang, P.D. Rack, *J. Vac. Sci. Technol. B*, 2008, **26**, 963–967. https://doi.org/10.1116/1.2917076

[22] A. Ganczarczyk, M. Geller, and A. Lorke, *Nanotechnology*, 2011, **22**, 045301. Doi: 10.1088/0957-4484/22/4/045301.

[23] M.G. Stanford, K. Mahady, B.B. Lewis, J.D. Fowlkes, S. Tan, R. Livengood, G.A. Magel, T.M. Moore, and P.D. Rack, *ACS Appl. Mater. Interfaces*, 2016, **8**, 29155–29162. https://doi.org/10.1021/acsami.6b09758

[24] J. Wang, D.P. Griffis, R. Garcia, and P.E. Russell, *Semicond. Sci. Technol.,* 2003, **18**, 199.

[25] J. Lasseter, S. Gellerup, S. Ghosh, S.J. Yun, R. Vasudevan, R.R. Unocic, O. Olunloyo, S.T. Retterer, K. Xiao, S.J. Randolph, and P.D. Rack, *ACS Appl. Mater. Interfaces,* 2024, **16**, 9144−9154. https://doi.org/10.1021/acsami.3c17182

[26] H.F. Winters and J.W. Coburn, *Appl. Phys. Lett.,* 1979, **34**, 70–73. https://doi.org/10.1063/1.90562

[27] T. Tachiki, K. Horiguchi, and T. Uchida, *Journal of Physics: Conference Series,* 2014, **507**, 042041. 10.1088/1742-6596/507/4/042041.

[28] V. Morosh, J. Linek, B. Müller, M.J. Martínez-Pérez, S. Wolter, T. Weimann, J. Beyer, T. Schurig, O. Kieler, A.B. Zorin, R. Kleiner, and D. Koelle, *Phys. Rev. Applied*, 2020, **14**, 054072. https://doi.org/10.1103/PhysRevApplied.14.054072

[29] V. Bouchiat, M. Faucher, C. Thirion, W. Wernsdorfer, T. Fournier, and B. Pannetier, *Appl. Phys. Lett*., 2001, **79**, 123-125. https://doi.org/10.1063/1.1382626

[30] S.O. Kasap, *Principles of Electronic Materials and Devices 3rd Edition*, McGraw-Hill Education, 2005.

[31] P. Marcon, and K. Ostanina, Overview of Methods for Magnetic Susceptibility Measurement, *Progress in Electromagnetics Research Symposium*, 2012.

[32] M.G. Castellano, R. Leoni, G. Torrioli, F. Chiarello, C. Cosmelli, A. Costantini, G. Diambrini-Palazzi, P. Carelli, R. Cristiano, and L. Frunzio, *J. Appl. Phys.*, 1996, **80**, 2922–2928. https://doi.org/10.1063/1.363147

[33] R. Vijay, E.M. Levenson-Falk, D.H. Slichter, and I. Siddiqi, *Appl. Phys. Lett., 2010,* **96**, 223112. https://doi.org/10.1063/1.3443716

[34] M. Jung, H. Noh, Y.-J. Doh, W. Song, Y. Chong, M.-S. Choi, Y. Yoo, K. Seo, N. Kim. B.-C. Woo, B. Kim, and J. Kim, *ACS Nano,* 2011, **5**, 2271–2276. https://doi.org/10.1021/nn1035679

[35] C. Granata, A. Vettoliere, P. Walke, E. Esposito, C. Nappi, P. Silvestrini, B. Ruggiero, and M. Russo, *J. Phys. Conf. Ser.* 2010*,* **234**, 042010. **DOI** 10.1088/1742-6596/234/4/042010

[36] R.H. Rai, A. Pérez-Pacheco, R. Quispe-Siccha, N.R. Glavin, and C. Muratore, *J. Vac. Sci. Technol. A,* 2020, **38**, 052201. doi: 10.1116/6.0000253.

[37] M.E. McConney, N.R. Glavin, A.T. Juhl, M.H. Check, M.F. Durstock, A.A. Voevodin, T.E. Shelton, J.E. Bultman, J. Hu, M.L. Jespersen, M.K. Gupta, R.D. Naguy, J.G. Colborn, A. Haque, P.T. Hagerty, R.E. Stevenson, and C. Muratore, *J. Mater. Res.,* 2016, **31**, 967–974. doi: 10.1557/jmr.2016.36.

[38] K. Kang, S. Xie, L. Huang, Y. Han, P.Y. Huang, K.F. Mak, C.-J. Kim, D. Muller, and J. Park, *Nature,* 2015, **520**, 656–660. https://doi.org/10.1038/nature14417

[39] D. Lagarde, L. Bouet, X. Marie, C.R. Zhu, B.L. Liu, T. Amand, P.H. Tan, and B. Urbaszek, *Phys. Rev. Lett.,* 2014, **112**, 047401. https://doi.org/10.1103/PhysRevLett.112.047401

[40] B. Radisavljevic, M. B. Whitwick, and A. Kis, *ACS Nano,* 2011, **5**, 9934–9938. https://doi.org/10.1021/nn203715c

[41] B. Radisavljevic, and A. Kis, *Nature Mater.*, 2013, **12**, 815–820. https://doi.org/10.1038/nmat3687

[42] K. Dolui, I. Rungger, and S. Sanvito, *Phys. Rev. B*, 2013, **87**, 075420. https://doi.org/10.1103/PhysRevB.88.075420

[43] U.P. Rathod, J. Egede, A.A. Voevodin, and N.D. Shepherd, *Appl. Phys. Lett.,* 2018, **113**, 062106. https://doi.org/10.1063/1.5040119

[44] M. G. Stanford, P. R. Pudasaini, E. T. Gallmeier, N. Cross, L. Liang, A. Oyedele, G. Duscher, M. Mahjouri-Samani, K. Wang, K. Xiao, D. B. Geohegan, A. Belianinov, B. G. Sumpter, P. D. Rack, *Adv. Funct. Mater.* 2017, **27**, 1702829. https://doi.org/10.1002/adfm.201702829

[45] M.G. Stanford, P.R. Pudasaini, A. Belianinov, N. Cross, J.H. Noh, M.R. Koehler, D.G. Mandrus, G. Duscher, A.J. Rondinone, I.N. Ivanov, T.Z. Ward, and P.D. Rack, *Sci Rep,* 2016, **6**, 27276. https://doi.org/10.1038/srep27276

[46] K.F. Mak, C. Lee, J. Hone, J. Shan, and T.F. Heinz, *Phys. Rev. Lett.*, 2010, **105**, 136805.

[47] E. Blundo, M. Felici, T. Yildirim, G. Pettinari, D. Tedeschi, A. Miriametro, B. Liu, W. Ma, Y. Lu, and A. Polimeni, *Phys. Rev. Research,* 2020, **2**, 012024(R). https://doi.org/10.1103/PhysRevResearch.2.012024

[48] M. Hosseini, M. Elahi, M. Pourfath, and D. Esseni, *IEEE Transactions on Electron Devices,* 2015, **62**, 3192 – 3198. DOI: 10.1109/TED.2015.2461617

[49] B. Sirota, N.R. Glavin, A.A. Voevodin, *Vacuum*, 2019, **160**, 133-138. https://doi.org/10.1016/j.vacuum.2018.10.077.

[50] B. Sirota, N. Glavin, S. Krylyuk, A.V. Davydov, and A.A. Voevodin*, Sci. Rep.,* 2018, **8**, 8668. doi: 10.1038/s41598-018-26751-4.

[51] G. Wang, Y. Zhang, C. You, B. Liu, Y. Yang, H. Li, A. Cui, D. Liu, and H. Yan, *Infrared Phys. Technol.,* 2018, **88**, 149–173. doi: 10.1016/j.infrared.2017.11.009.

[52] Y. Xue, Y. Zhang, Y. Liu, H. Liu, J. Song, J. Sophia, J. Li, Z. Xu, Q. Xu, Z. Wang, J. Zheng, Y. Liu, S. Li, and Q. Bao, *ACS Nano*, 2016, **10**, 573–580. doi: 10.1021/acsnano.5b05596.

[53] N.R. Glavin, C. Muratore, and M. Snure, *Oxf. Open Mater. Sci.,* 2020, **1**, itaa002. doi: 10.1093/oxfmat/itaa002

[54] C.W. Lee, J.M. Suh, and H.W. Jang, *Front. Chem.,* 2019, **7**, 708. doi: 10.3389/fchem.2019.00708.

[55] P. Feng, E. Chavez, and C. Malca, *Chemosensors*, 2018, 6, no. 4, p. 49, Nov. 2018, doi: 10.3390/chemosensors6040049.

[56] D. Voiry, J. Yang, and M. Chhowalla, *Adv. Mat.,* 2016, 28, 6197-6206. https://doi.org/10.1002/adma.201505597

[57] D.M. Khaidar, W.N.R.W. Isahak, Z.A.C Ramli, and K.N. Ahmad, *Hydrogen Energy*, 2024, **68**, 35-50. https://doi.org/10.1016/j.ijhydene.2024.04.220

[58] G.W. Shim, W. Hong, S.Y. Yang, and S.-Y. Choi, *J. Mater. Chem. A*, 2017, **5**, 14950-14968.I https://doi.org/10.1039/C7TA03039H

[59] H. Qi, L. Wang, J. Sun, Y. Long, P. Hu, F. Liu, and X. He, *Crystals*, 2018; **8**, 35. https://doi.org/10.3390/cryst8010035

[60] Australian Microscopy and Microanalysis Research Facility, “My Scope-training for advanced research” http://www.ammrf.org.au/myscope/sem/background/

[61] Kabita Sharma, Atomic Force Microscopy: Principle, Instrumentation, Advantages, Applications, 2023, https://scienceinfo.com/atomic-force-microscopy-instrumentation/

[62] *Analytical Methods in Geosciences*, by Elizabeth A. Johnson, Juhong Christie Liu, and others, CC-BY-SA. https://viva.pressbooks.pub/analyticalmethodsingeosciences/

[63] P. Das, C.V. Tomy, S.S. Banerjee, H. Takeya, S. Ramakrishnan, and A.K. Grover, *Phys. Rev. B*, 2008, **78**, 214504. https://doi.org/10.1103/PhysRevB.78.214504

[64] R. Prozorov, M. Zarea, and J.A. Sauls, *Phys. Rev. B*, 2022, **106**, L180505. https://doi.org/10.1103/PhysRevB.106.L180505\

[65] J. Wang, D.P. Griffis, R. Garcia, and P.E. Russell, *Semicond. Sci. Technol.*, 2003, **18**, 199. https://doi.org/10.1116/1.1848107

[66] F.J. Schoenaker, R. Córdoba, R. Fernández-Pacheco, C. Magén, O. Stéphan, C. Zuriaga-Monroy, M.R. Ibarra, and J.M. De Teresa, *Nanotechnology,* 2011, **22**, 265304. doi:10.1088/0957-4484/22/26/265304

[67] A. Kumar, K.N. Nazif, P. Ramesh, and K. Saraswat, *2020 Device Research Conference (DRC)*, Columbus, OH, USA, 2020, 1-2, doi: 10.1109/DRC50226.2020.9135155.

[68] R. Zhang, D. Drysdale, V. Koutsos, R. Cheung, *Adv. Funct. Mater.* 2017, **27**, 1702455. https://doi.org/10.1002/adfm.201702455

[69] V. Kaushik, M. Ahmad, K. Agarwal, D. Varandani, B.D. Belle, P. Das, and B.R. Mehta, *The Journal of Physical Chemistry C,* 2020*,* **124**, 23368-23379. DOI: 10.1021/acs.jpcc.0c05651

[70] W. Wu, Q. Zhang, X. Zhou, L. Li, J. Su, F. Wang, and T. Zhai, *Nano Energy*, 2018, **51**, 45-53. https://doi.org/10.1016/j.nanoen.2018.06.049.

[71] X. Hong, J. Kim, S.-F. Shi, Y. Zhang, C. Jin, Y. Sun, S. Tongay, J. Wu, Y. Zhang, and F. Wang, *Nature Nanotech,* 2014, **9**, 682–686. https://doi.org/10.1038/nnano.2014.167

[72] J. Zhang, J. Wang, P. Chen, Y. Sun, S. Wu, Z. Jia, X. Lu, H. Yu, W. Chen, J. Zhu, G. Xie, R. Yang, D. Shi, X. Xu, J. Xiang, K. Liu, and G. Zhang, *Adv. Mater.,* 2016, **28**, 1950-1956. https://doi.org/10.1002/adma.201504631

[73] N. Huo, J. Kang, Z. Wei, S.-S. Li, J. Li, and S.-H. Wei, *Adv. Funct. Mater.,* 2014, **24**, 7025-7031. https://doi.org/10.1002/adfm.201401504

[74] Y. Gong, J. Lin, X. Wang, G. Shi, S. Lei, Z. Lin, X. Zou, G. Ye, R. Vajtai, B.I. Yakobson, H. Terrones, M. Terrones, B.K. Tay, J. Lou, S.T. Pantelides, Z. Liu, W. Zhou, and P.M. Ajayan, *Nature Mater,* 2014, **13**, 1135–1142. https://doi.org/10.1038/nmat4091

[75] X.Q. Zhang, C.H. Lin, Y.-W. Tseng, K.-H. Huang, and Y.-H. Lee, *Nano Lett.,* 2015**, 15**, 410. doi: 10.1021/nl503744f

[76] K. Chen, X. Wan, J. Wen, W. Xie, Z. Kang, X. Zeng, H. Chen, and J.-B. Xu, *ACS Nano*, 2015, **9**, 9868. doi: 10.1021/acsnano.5b03188

[77] D. Cao, T. Shen, P. Liang, X. Chen, and H. Shu, *J. Phys. Chem. C*, 2015 **8**, 4294. doi: 10.1021/jp5097713

[78] C. Martella, L. Ortolani, E. Cianci, A. Lamperti, V. Morandi, and A. Molle, *Nano Res., 2019,* **12**, 1851–1854. https://doi.org/10.1007/s12274-019-2446-0